This is a postprint version of the following published document:

Modeling and Performance of Electrodynamic Low-Work-Function Tethers with Photoemission Effects

G. Sanchez-Arriaga* and Xin Chen†

Universidad Carlos III de Madrid, Leganés 28911, Spain

DOI: 10.2514/1.B36561

A low-work-function tether is a long conductor coated with a low-work-function material that orbits around a planet with both the magnetic field and ionosphere. Depending on the work function W of the coating and the tether temperature T, the photoelectron emission can be relevant within the cathodic tether segment. Thus, this mechanism needs to be added to the thermionic emission considered in previous works. An emission model for low-work-function tethers, including a typical solar photon spectrum, a Fowler–DuBridge law for the photoelectron yield of the coating, and a Richardson–Dushman law for the thermionic emission, is presented, and used to organize the thermionic and photoelectric dominated regimes of low-work-function tethers within the W–T plane. For $T \approx 500$ K and $W \approx 1.5$ eV, the photoemission and thermionic emission can be of the same order and have similar efficiency as the electron collection. The emission model is combined with orbital-motion theory for all the plasma and emitted particles, and the longitudinal bias and current profiles throughout a low-work-function tether are determined for typical low-Earth-orbit environmental values. Results for the average current are presented. The study highlights the main electrical, mechanical, and optical properties that should be considered in the design of low-work-function tethers, and it briefly discusses some promising materials.

Nomenclature

A_t	=	tether cross-sectional area, m^2
B	=	ambient magnetic field, T
E_m	=	motional electric field along the tether, V/m
E	=	photon energy, eV
e	=	elementary charge, C
F_L	=	Lorentz force, N
f_α	=	distribution function of particle α, s^2/m^5
h_p	=	Planck constant, m$^2 \cdot$ kg/s
I	=	current along the tether, A
J	=	current density, A/m^2
k_B	=	Boltzmann constant, m$^2 \cdot$ kg/s^2 K
L_t	=	tether length, m
L^*	=	length characterizing ohmic effects, m
M_s	=	spacecraft mass, kg
m_e	=	electron mass, kg
m_t	=	tether mass, kg
N_0	=	ambient plasma density, 1/m^3
p_t	=	tether perimeter, m
R	=	tether radius, m
r_s	=	orbital radius of the spacecraft, m
S	=	solar energy spectrum, ph/sm^2 eV
S_{Sun}	=	solar constant, W/m^2
T_e	=	electron temperature, K
T_{eq}	=	tether equilibrium temperature, K
T_i	=	ion temperature, K
T_m	=	melting temperature, K
u_t	=	unit vector along the straight tether
v	=	tether-to-plasma relative velocity, m/s
W	=	work function, eV
x	=	distance along tether from its anodic end, m
Y_{ph}	=	tether photoelectron yield (electrons per incoming photon)
α_{abs}	=	tether solar absorption
ϵ_{em}	=	tether emissivity
λ_{De}	=	electron Debye length, m
μ	=	standard gravitational parameter, m^3/s^2
ρ_t	=	tether density, kg/m^3
ρ_0	=	tether radius to Debye length ratio
σ_B	=	Stefan–Boltzmann constant, W/m$^2 \cdot$ K^4
σ_t	=	tether conductivity, 1/Ωm
Φ_p	=	tether-to-plasma bias, V
ϕ_F	=	Fowler function

Subscripts

ph	=	photoelectric
t	=	tether
th	=	thermionic

I. Introduction

THE space debris population near the Earth will increase in the future due to new launches, on-orbit explosions, and accidental collisions. Even without future launches, studies show that the low-Earth-orbit (LEO) debris population will remain relatively constant for the next four decades and will increase noticeably beyond that [1,2]. Effective means to protect the environment include the deorbit of satellites, payload adapters, and rocket stages at their end of life and the active debris removal of the most dangerous objects. Both actions require an active deorbit technology, like chemical and electrical thrusters, or a passive technology, like drag augmentation devices and electrodynamic tethers in passive mode [3–5].

Bare electrodynamic tethers equipped with plasma contactors, introduced in 1993 [6], can provide a relatively simple and effective solution within a wide range of orbits and spacecraft masses [7–9]. As compared with other technologies, this device has important advantages, which would be enhanced even more if the plasma contactor and its expellant were eliminated. Pursuing this idea, the bare thermionic tether was introduced in 2012 [10]. If the tether is coated with a low-work-function material, then the cathodic contact with the ambient plasma is accomplished by thermionic emission from the tether itself. The operation of such a tether is fully passive and, in deorbit scenarios, does not involve consumables and power. One of the main advantages of using the tether itself for anodic and cathodic contacts is to allow a large collecting/emitting area (even for small tether radius or width) and the reduction of space-charge effects. A preliminary analysis showed that the thermionic tether is a

*Ramón y Cajal Research Fellow, Bioengineering and Aerospace Engineering Department, Avda. de la Universidad 30, Madrid.

†Visiting Professor (Postdoctoral), Bioengineering and Aerospace Engineering Department, Avda. de la Universidad 30, Madrid.

promising device for a deorbit payload adapter from geostationary transfer orbits [11].

The charge exchanges between the tether and the ambient plasma and the longitudinal current and voltage profiles along the tether are the main components of the electrical model of the thermionic tether. For an orbital velocity v, the magnetic field B induces, on the tether reference frame, a motional electric field $v \times B$, which drives an electric current along the tether if a closed-circuit electric contact with the environmental plasma is provided. Cathodic and anodic segments develop along such an electrically floating thermionic tether. The tether collects electrons along the anodic segment as a giant Langmuir probe, and the cathodic segment emits electrons as a giant emissive probe. However, the modeling of the latter is more complex and involves the physical properties of the coating and the ambient plasma.

The first work on thermionic tethers ignored ohmic effects and showed that, in general, the cathodic tether segment had two regions [10] (see Fig. 1): 1) a segment with space-charge-limited (SCL) emission that extends from the zero bias point B up to an intermediate point B^*, and 2) a segment between B^* and the tether cathodic end C with full Richardson–Dushman (RD) thermionic emission. The device is said to operate in the short-tether regime when the full cathodic segment is SCL and in the long-tether regime if both SCL and RD segments exist. Preliminary models for the precise location of B^* and the plasma/tether charge exchange within BB^* were used in [10]. A later analysis included ohmic effects [12]. In [13], a more refined model based on orbital-motion theory (OMT) [14,15] for the location of B^* was used, and the organization of the short- and long-tether operational regimes were discussed in terms of two key dimensionless parameters.

All the previous works on bare tethers coated with low-work-function materials considered thermionic emission at the cathodic segment. However, our analysis shows that, thanks to the coating, the tether can also act as a photocathode under the natural illumination of the Sun. In 1965, photoelectron emission was mentioned for the first time in the pioneer work on electrodynamic tethers by Drell et al. [16] as a mechanism to close the tether–plasma current circuit. However, to the best of our knowledge, our work is the first that presents a model for bare tethers with photoemission at the cathodic segment. Whether photoelectron emission is negligible, comparable, or dominant to thermionic emission basically depends on tether properties like work function, photoelectric yield, and temperature. For this reason, we will refer to the device as a low-work-function tether, or low-W tether (LWT), instead of a thermionic or photoelect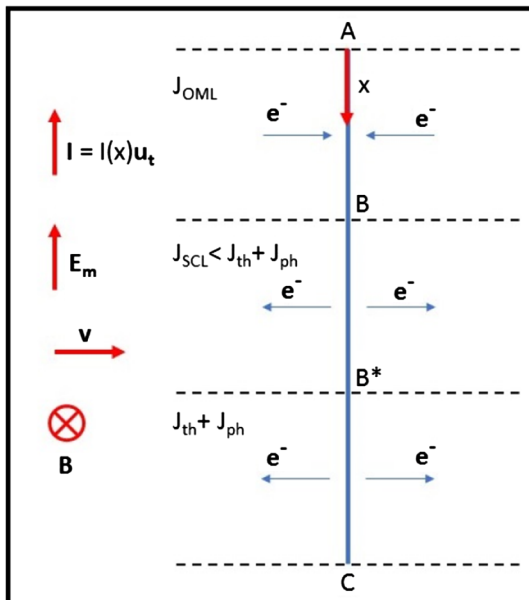ric tether. The second novelty of the work is related with the tether/plasma current exchange model, which incorporates full numerical solutions of the Vlasov–Poisson system. This contribution allows us to make an assessment of the approximate analytical model used in previous works [10,12].

The work is organized as follows. Section II.A introduces a photoemission model for the LWT and discusses the operational regimes as a function of the work function and the tether temperature. In Sec. II.B, we modify a recent model for emissive and Langmuir probes [17] to incorporate photoelectric effects. For both anodic and cathodic segments, the current density versus tether bias characteristics $J(\Phi_p)$ are found by self-consistently solving the Vlasov–Poisson system, considering both thermionic and photoelectric effects. The relations $J(\Phi_p)$ obtained numerically are used to determine the efficiency of LWTs in deorbit scenarios, as well as to make a critical comparison with previous works. Promising materials for LWT applications are discussed in Sec. IV. The conclusions are summarized in Sec. V.

II.   Low-Work-Function Tethers Model

For a tether of length L_t, conductivity σ_t, cross-sectional area A_t, and perimeter p_t, the longitudinal profiles of the current intensity $I(x)$ and the tether-to-plasma bias $\Phi_p(x)$ are governed by [6]

$$\frac{dI}{dx} = p_t J(\Phi_p) \tag{1}$$

$$\frac{d\Phi_p}{dx} = \frac{I}{\sigma_t A_t} - E_m \tag{2}$$

where $J(\Phi_p)$ is the collected/emitted current density (positively defined for electron collection); $x \in [0, L_t]$ is the distance along tether from its anodic tip; and $E_m = \boldsymbol{u}_t \cdot (\boldsymbol{v} \times \boldsymbol{B})$ is the motional electric field projection along $\boldsymbol{u}_t$, which is the tangent unit vector along the straight tether pointing in the direction of the electric current $[\boldsymbol{I} = I(x)\boldsymbol{u}_t]$. Given the law $J(\Phi_p)$, the integration of Eqs. (1) and (2) with the boundary conditions $I(0) = I(L_t) = 0$ provides the current intensity and bias profiles. From them, one finds the Lorentz force

$$\boldsymbol{F}_L = \int_0^{L_t} \boldsymbol{u}_t \times \boldsymbol{B} I(x) \, dx \approx \boldsymbol{u}_t \times \boldsymbol{B} \int_0^{L_t} I(x) \, dx \tag{3}$$

which mainly governs the deorbit performance of the device.

Therefore, the key aspect in the modeling of the tether is the relationship $J(\Phi_p)$ that is inserted in Eqs. (1) and (2). For the anodic segment, previous works [6,10] used the orbital-motion-limited (OML) current law. Analytical formulas in the classical [18] and the relativistic [19] (if the probe bias is extremely high, like in Jupiter) regimes can be used for a tether radius R below a threshold [20]. In the high bias limit ($e\Phi_p/k_B T_e \gg 1$, with T_e as the plasma electron temperature and k_B as the Boltzmann constant), it reads

$$J_{OML} = \frac{eN_0}{\pi} \sqrt{2e\Phi_p/m_e} \tag{4}$$

where m_e is the electron mass, e is the electron charge, and N_0 is the unperturbed plasma density. For the cathodic segment, past works considered three basic mechanisms. Each ion impacting on the cathodic segment picks up an electron to leave as neutral. Depending on the tether bias, this rate can be increased by secondary electron emission. The emission due to these two mechanisms reads

$$J_{\text{ion+sec}} = -\frac{eN_0}{\pi} \sqrt{2e\Phi_p/m_i}(1 + \gamma_1|\Phi_p|) \tag{5}$$

with γ_1 the yield written per unit bias. They were both discussed in [21], where a cathodeless bare tether was proposed to excite artificial auroral effects. A typical value of $\gamma_1 = 0.15/kV$ was used for the modeling of the secondary electron emission. As a consequence of the ion mass in the denominator of Eq. (5), these two current densities

Fig. 1   Schematics of a LWT (adapted from [10,12]).

were small as compared to the electron collection (for equal bias) in the anodic segment given by Eq. (4). For O^+ ions, the ratio between the two currents is $\sqrt{m_e/m_i} \approx 1/172$. In deorbiting scenarios, the performance of such a floating tether would be very low. For this reason, recent works considered a tether coated with a low-work-function material [10,12,15], which emitts electrons thermionically and follows the Richardson–Dushman law

$$J_{\text{th}} = -AT^2 \exp\left(-\frac{W}{k_B T}\right) \quad (6)$$

with

$$A = \frac{4\pi m_e e k_B^2}{h_p^3} \approx 1.20 \cdot 10^6 \ \text{Am}^{-2}\,\text{K}^{-2}$$

where h_p is the Planck constant; and T and W are the temperature and work function of the tether, respectively. For relevant values of W/T, one has $J_{\text{OML}} \sim |J_{\text{th}}| \gg |J_{\text{ion+sec}}|$; i.e., the ion collection and secondary emission can be ignored. As shown in Sec. II.A, there is a fourth mechanism (photoemission) that can compete with thermionic emission.

Along the cathodic segment, the evaluation of the emitted current from the tether to the plasma becomes more complicated due to space-charge effects. Emitted electrons result in a negative space charge, which suppresses the electric field that accelerates the emitted electrons outward, or even reverses it at segment BB^* in Fig. 1. Currents emitted by the points at this segment are space-charge-limited, with a current density of $|J_{\text{SCL}}| < |J_{\text{th}}|$. Previous works [10,15] used a crude model for J_{SCL}, and [15] presented an asymptotic analysis to predict the position of B^* using the OML theory.

A. Photoelectric Emission by LWTs

A coating with low-W materials does not only ease the thermionic electron emission but can also yield to a relevant photoemission level. The cathodic tether segment, with a negative bias with respect to the ambient plasma, can act as a passive photocathode under the natural illumination of the Sun. However, the modeling of the photocurrent for metal surfaces coated with low-W materials is a difficult and complex task. The photon absorption, the transport of the electrons to the surface, and the emission are affected by several factors, including the band structure of the metal, the thickness of the coating, and the angle of incidence and polarization of the light, among others [22]. A reliable determination of the photocurrent, which is highly dependent on the chosen metal/coating combination and the surface treatment, typically requires experiments. In this work, we used a relatively simple but general model and verified that the results were in agreement with previous experiments for specific materials.

The current density of photoelectrons (A/m²) is given by

$$J_{\text{ph}} = -f(1 - r_t)e \int_0^\infty S(E) Y_{\text{ph}}(E)\,\mathrm{d}E \quad (7)$$

where r_t is the LWT reflectivity; the energy spectrum of the solar photons $S(E)$ is the number of photons per unit of time, area and energy (with units of ph/sm² eV); and $Y_{\text{ph}}(E)$ is the photoelectric yield of the LWT, i.e., the number of emitted electrons (hereafter shown as "el") per incoming photon (hereafter shown as "photon (ph)") for a given photon energy E. The factor f takes into account that only a fraction of the total perimeter is illuminated by the sun. Figure 2a shows the energy spectrum $S(E)$, including the continuous spectrum (solid line) and the spectral lines (triangles), versus the photon energy in electron volts. For energies below and above 4.8 eV, we used the 2000 ASTM Standard Extraterrestrial Spectrum Reference E-490-00 [23] and the data from [24], respectively. For the case of interest of this work (i.e., LWTs with work functions below about 1.5 eV), the photocurrent contribution coming from the portion of the solar spectrum above 5 eV was small (below few a percent of the total).

Regarding the photoelectric yield $Y_{\text{ph}}(E)$ in Eq. (7), we adopted the Fowler–DuBridge law [25,26]:
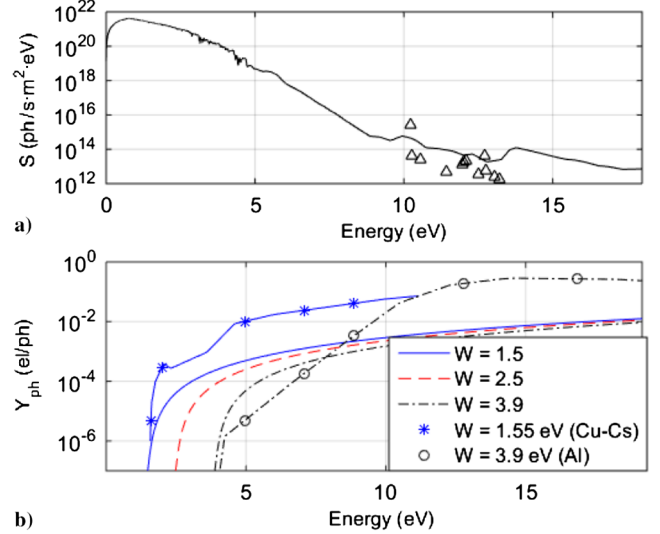

Fig. 2 Panels a) and b) show the solar photon spectrum and the photoelectric yield, respectively.

$$Y_{\text{ph}}(E) = \alpha A T^2 \phi_F\left(\frac{E - W}{k_B T}\right) \quad (8)$$

where ϕ_F is the Fowler function

$$\phi_F(x) = \begin{cases} e^x - \frac{e^{2x}}{2^2} + \frac{e^{3x}}{3^2} + \ldots & x \leq 0 \\ \frac{x^2}{2} + \frac{\pi^2}{6} - \left(e^{-x} - \frac{e^{-2x}}{2^2} + \frac{e^{-3x}}{3^2} - \ldots\right) & x \geq 0 \end{cases} \quad (9)$$

with α as a constant that depends on the material. For metals, α is typically between 5×10^{-19} and 5×10^{-18} el $\cdot$ m²/ph $\cdot$ A. Hereafter, we will (conservatively) assume $\alpha \approx 5.10^{-19}$ el $\cdot$ m²/ph $\cdot$ A. Interestingly, the Richardson–Dushman law [Eq. (6)] and the Fowler–DuBridge photoelectric yield [Eq. (8)] have a similar dependence with the temperature and the work function.

Figure 2b shows the photoelectric yield per incoming photon versus photon energy using the Fowler–DuBridge law and for work function values of $W = 1.5$, 2.5, and 3.9 eV. The lines with stars and with circles correspond to the experimental data of copper (Cu) with a monolayer of cesium (Cs) on the surface and aluminum (Al) oxide, adapted from [27,28], respectively. For these materials, the authors found work function values equal to 1.55 and 3.9 eV. As shown in the figure, the Fowler–DuBridge law gives a first approximation of $Y_{\text{ph}}(E)$, but accurate and reliable values of $Y_{\text{ph}}(E)$ require experimental tests with the specific metal, coating, and surface treatment. For $W = 1.5$ eV, our model is very conservative, i.e., it predicts a low value of photoelectrons because the experimental curve of $Y_{\text{ph}}(E)$ is more than one order of magnitude above the theoretical one. For 3.9 eV, the model is optimistic (conservative) for energies below (above) about 8 eV.

Unfortunately, experimental data of the photoelectric yields for the most promising materials with applications to LWTs (see Sec. IV) are not available yet. This issue introduces uncertainties in the results that we mitigated by presenting parametric studies that vary the LWT temperature and its work function. Figure 3 shows the sum of the photoelectric and the thermionic density currents in a logarithm scale versus these two design parameters. The calculation was carried out with Eqs. (6–8), $f = r_t = 1/2$, and the solar flux shown in Fig. 2. The W–T relation that gives $J_{\text{th}} = J_{\text{ph}}$ is shown with a dashed black curve. It separates the parametric domains where the current emission is dominated by photoemission or thermionic emission.

For typical plasma and LWT conditions in LEO ($N_0 = 10^{11}$ m⁻³ and $E_m = 150$ V/km), Eq. (4) shows that the maximum collected electron current density for a 1-km-length anodic segment is about $J_{\text{OML}} \approx 3.6 \cdot 10^{-2}$ A/m² ($\Phi_p \approx E_m L$). Curiously, according to Fig. 3, a LWT with an emission level about this order of magnitude
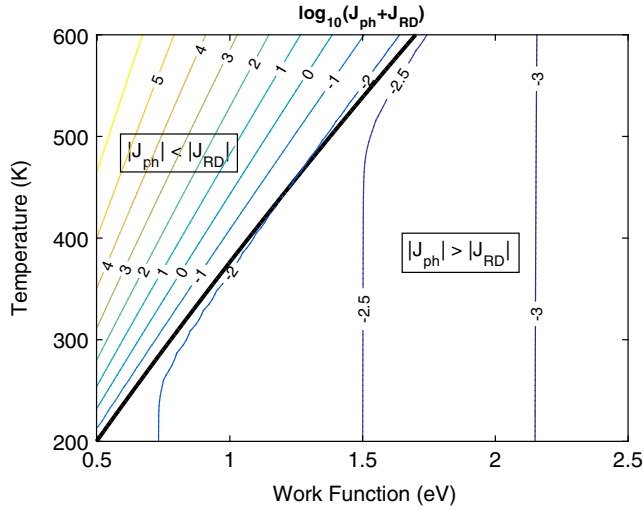
Fig. 3   Contour plot of $\log_{10}(|J_{ph} + J_{th}|)$ versus T and W (J in amperes per square meter).

(i.e., $|J_{ph} + J_{th}| \sim 10^{-2}$ A/m²) has similar contributions from thermionic and photoelectric emissions. Figure 3 also reveals the high sensitivity of the LWT performance with the temperature and the work function. Regarding the former, a balance between radiative cooling and solar absorption gives the LWT equilibrium temperature

$$T_{eq} = \left(\frac{\alpha_{abs} S_{Sun}}{\pi \epsilon_{em} \sigma_B} \right)^{1/4} \qquad (10)$$

with α_{abs} and ϵ_{em} as the tether absorptivity and emissivity, $S_{Sun} \approx$ 1.37 kW/m² as the solar constant, and $\sigma_B \approx 5.67 \cdot 10^{-8}$ W/m² K⁴ as the Stefan–Boltzmann constant. For $\alpha_{abs} = 0.5$ and $\epsilon_{em} = 0.06$, one finds $T_{eq} \approx 500$ K. Joule heating, ignored by this first balance, would increase the equilibrium temperature even more.

B.   Plasma/LWT Contact

Because the typical length of the LWT is several kilometers and its radius R is about a few millimeters, condition $L_t \gg R$ holds. For tapes, the width w_t also satisfies $L_t \gg w_t$. This simplifies the LWT/plasma contact model notably because the current density J of a LWT cross section at a particular bias Φ_p can be analyzed as a two-dimensional uniformly biased Langmuir probe. It is well known from probe theory that J in Eq. (1) does not generally coincide with J_{OML} and the sum $J_{ph} + J_{th}$ in the anodic and the cathodic segments, respectively. Depending on the LWT properties and environmental parameters, a tether cross section could collect electrons beyond the OML regime ($J < J_{OML}$) or emit current under SCL conditions ($|J| < |J_{th} + J_{ph}|$).

A rigorous determination of $J(\Phi_p)$ requires the OMT, which corresponds to self-consistent solutions of the stationary Vlasov–Poisson system in cylindrical coordinates. In a recent work, this problem was written as an ordinary integrodifferential equation and $J(\Phi_p)$ relations were computed numerically for both positive and negative biases [17]. As will be explained in the following (see also the Appendix), minor modifications are required to adapt this theory to LWT applications with photoelectric effects.

The first change is related with the boundary conditions of the distribution functions, which should include the photoelectrons. At the faraway plasma ($r \to \infty$), the electron and ion plasma distribution functions are assumed to be Maxwellian:

$$f_{e,i}(r \to \infty, v_r, v_\theta) = \frac{N_0 m_{e,i}}{2\pi k_B T_{e,i}} \exp\left[-\frac{m_{e,i}(v_r^2 + v_\theta^2)}{2k_B T_{e,i}} \right] \qquad (11)$$

with v_r and v_θ as the radial and azimuthal velocities, and r as the radial distance from the probe axis. At the LWT ($r = R$), the distribution functions of the emitted electrons are assumed to be half-Maxwellian:

$$f_{ph,th}(R, v_r > 0, v_\theta) = \frac{N_{0ph,th} m_e}{\pi k_B T_{ph,th}} \exp\left[-\frac{m_e(v_r^2 + v_\theta^2)}{2k_B T_{ph,th}} \right] \qquad (12)$$

where subscripts ph and th denote electrons emitted through photoelectric and thermionic effects, respectively. For thermionic emission, we take $T_{th} = T$ in Eq. (12), as is commonly done in emissive Langmuir probe studies. Regarding photoemission, an isotropic distribution is realistic for amorphous materials but would not necessarily hold for finely powdered substances [28]. For materials with $W \sim 4$–5 eV, like aluminum (Al) oxide, the mean kinetic energy is about $k_B T_{ph} \approx 1$ eV [28]. However, experimental results for copper coated with cesium ($W = 1.55$ eV) indicate that the mean kinetic energy could be lower [27]. Our calculations will consider $k_B T_{ph} \approx 0.25$ eV.

Taking into account [17] and Eqs. (11) and (12), the OMT for a probe with thermionic and photoelectric emissions depends on the following dimensionless parameters

$$\delta_i \equiv \frac{T_i}{T_e}, \qquad \delta_{th} \equiv \frac{T_{th}}{T_e}, \qquad \delta_{ph} \equiv \frac{T_{ph}}{T_e}, \qquad \varphi_p \equiv \frac{e\Phi_p}{k_B T_e} \qquad (13)$$

$$\rho_0 \equiv \frac{R}{\lambda_{De}}, \qquad \beta_{th} \equiv \frac{N_{0th}}{N_0}, \qquad \beta_{ph} \equiv \frac{N_{0ph}}{N_0} \qquad (14)$$

with λ_{De} as the electron Debye length. From Eq. (12), one finds the relation

$$J_{ph} = -e \int_0^\infty \int_{-\infty}^{+\infty} v_r f_{ph} \, dv_r \, dv_\theta = -N_{0ph} e \sqrt{\frac{2k_B T_{ph}}{\pi m_e}} \qquad (15)$$

and a similar equation holds if subscript ph is changed by th. Because J_{th} and J_{ph} are given by Eqs. (6) and (7), the ratios β_{th} and β_{ph} are related with LWT properties: W, T, and $Y_{ph}(E)$.

Given the set of parameters in Eqs. (13) and (14), the current density $J(\Phi_p)$ appearing in Eq. (1) is computed as follows. First, the normalized potential profile $\varphi(\rho) = e\Phi/kT_e$ is found by solving Poisson equation

$$\frac{1}{\rho} \frac{d}{d\rho}\left(\rho \frac{d\varphi}{d\rho} \right) = -\rho_0^2(n_i - n_e - \beta_{ph} n_{ph} - \beta_{th} n_{th}) \qquad (16)$$

with $\rho = r/R$. The stationary Vlasov equation with an axisymmetric geometry (round LWT) conserves the energy, the angular momentum, and the distribution function; and this can be used to write the normalized particle densities $n_\alpha(\rho)$ as integrals involving $\varphi(\rho)$ (see details in the Appendix and [17]). Equation (16), with the boundary conditions $\varphi(\rho = 1) = \varphi_p$ and $\varphi \to 0$ as $r \to \infty$, is an integrodifferential equation that is solved with an iterative numerical algorithm. Once the potential profile $\varphi(\rho)$ is known, the normalized current density $j_{LWT} \equiv J/J_0$ is computed from Eq. (A7), with $J_0 = eN_0 \sqrt{k_B T_e/2\pi m_e}$ as the random electron thermal current.

As an example, we now consider typical environmental values in LEO: $k_B T_e = k_B T_i = 0.15$ eV, $E_m = 150$ V/km, oxygen ions, and LWT properties: $R = 1$ mm, $r_t = f = 1/2$, $T = 500$ K, $k_B T_{th} = k_B T$, and $k_B T_{ph} = 0.25$ eV. These values give the dimensionless parameters $\delta_i = 1$, $\delta_{th} \approx 0.29$, $\delta_{ph} \approx 1.7$, and $\mu_i \approx 29378$. Three relevant cases of plasma densities and coating work functions are studied (see Table 1): 1) $N_0 = 10^{11}$ m⁻³ and $W = 1.4$ eV ($\rho_0 \approx 0.11$, $\beta_{th} \approx 2.1$, and $\beta_{ph} \approx 1.4$), 2) $N_0 = 10^{12}$ m⁻³ and $W = 1.4$ eV ($\rho_0 \approx 0.35$, $\beta_{th} \approx 0.21$, and $\beta_{ph} \approx 0.14$), and 3) $N_0 = 10^{12}$ m⁻³ and $W = 1.2$ eV ($\rho_0 \approx 0.35$, $\beta_{th} \approx 21.6$, and $\beta_{ph} \approx 0.19$). In cases 1 and 2, thermionic and photoelectric effects are comparable, whereas in case 3 (the one with the higher emission level), thermionic emission is dominant.

Table 1   Parameter considered in the analysis

Case	N_0, m^{-3}	W, eV	ρ_0	β_{th}	β_{ph}
1	10^{11}	1.4	0.11	2.1	1.4
2	10^{12}	1.4	0.35	0.21	0.14
3	10^{12}	1.2	0.35	21.6	0.19

For these three cases, we computed the j_{LWT}–φ_p curve with the Vlasov–Poisson solver (see solid curves in Fig. 4) and with the analytical model presented in [12], but improved with the photoelectric effect (dashed lines). A detail of this diagram close to the origin is shown in Fig. 5. The segment of the j_{LWT}–φ_p curve between the two crosses operates under SCL conditions (nonmonotonic potential). As expected, both models match very well, except close to the origin due to space-charge effects. Section III discusses the importance of such a discrepancy on tether performance and shows that the simplified model of [10] is adequate for preliminary mission design within a wide range of conditions.

Previous calculations are valid for round tethers at rest and negligible trapped particle populations. Note that the angular momentum of the particles is not conserved for tape tethers or if the relative motion between the plasma and the tether–plasma is considered. Trapped particles arise due to collisions or transient phenomena, which would lead to the breakdown of the conservation
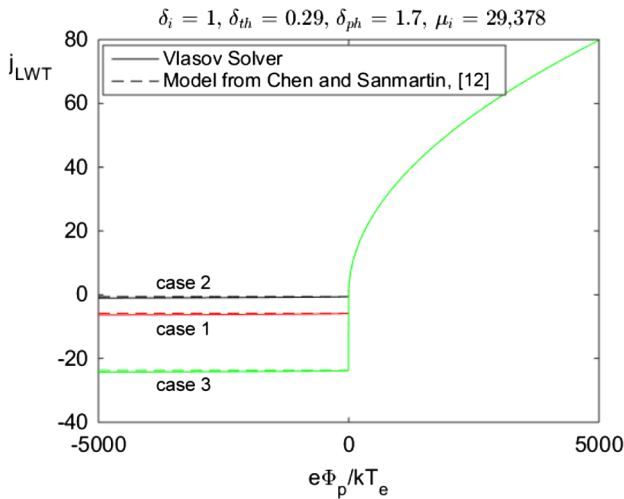
Fig. 4   Normalized current j_{LWT} versus normalized probe bias φ_p for several emission levels.
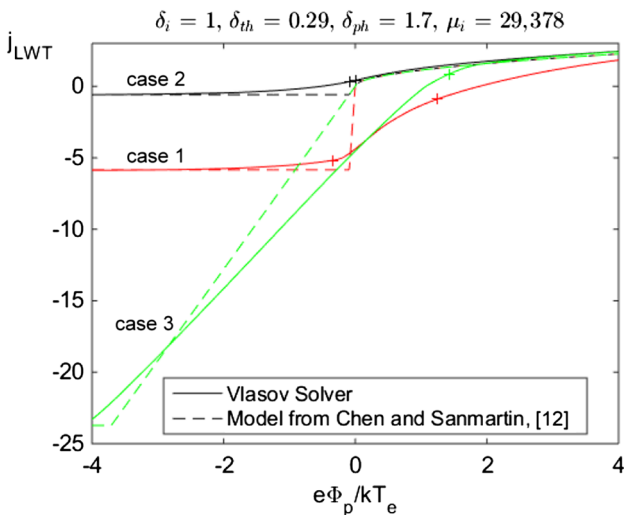
Fig. 5   Normalized current j_{LWT} versus normalized probe bias φ_p for several emission levels.

of f_α or the energy, respectively. Accurate $J(\Phi_p)$ relations for these conditions require the extension of computationally demanding codes like the one presented in [29–31].

III.   Electrodynamic Performance

After introducing the dimensionless variables $i \equiv I/E_m \sigma_t A_t$, $\phi \equiv \Phi_p/E_m L_t$, and $\xi \equiv x/L_t$, Eqs. (1) and (2) become

$$\frac{\mathrm{d}i}{\mathrm{d}\xi} = \lambda j_{LWT}(\phi), \qquad \frac{\mathrm{d}\phi}{\mathrm{d}\xi} = i(\xi) - 1 \tag{17}$$

where $\lambda \equiv L_t/L_0$ and

$$L_0 \equiv E_m \sigma_t A_t / p_t e N_0 \cdot \sqrt{2\pi m_e/k_B T_e}$$

The integration of this set of equations, with the boundary conditions $i(0) = i(1) = 0$ and $j_{LWT}(\varphi_p)$ given by Eq. (A7), provides the current and voltage profiles along the tether (note that $\varphi_p = \phi e E_m L_t/kT_e$). Once $i(\xi)$ is known, one computes the normalized average current

$$i_{av} = \int_0^1 i(\xi)\,\mathrm{d}\xi = 1 + \phi(1) - \phi(0) \tag{18}$$

that naturally appears in the Lorentz force [see Eq. (3)]:

$$\boldsymbol{F}_L \approx E_m \sigma_t A_t L_t i_{av}(\boldsymbol{u}_t \times \boldsymbol{B}) \tag{19}$$

The dot product of the spacecraft velocity $\boldsymbol{v} = \mathrm{d}\boldsymbol{r}_s/\mathrm{d}t$ with its equation of motion $\mathrm{d}\boldsymbol{v}/\mathrm{d}t = -\mu \boldsymbol{r}_s/r_s^3 + \boldsymbol{F}_L/M_s$ yields [9]

$$\frac{\mathrm{d}r_s}{\mathrm{d}t} = -2\frac{r_s^2}{\mu}\frac{m_t}{M_s}\frac{\sigma_t}{\rho_t}E_m^2 i_{av} \tag{20}$$

where we assume that the Lorentz drag makes the orbit slowly evolve through a sequence of quasi-circular orbits with $v^2 \approx \mu/r_s$, and the straight tether is perfectly aligned with the local vertical. In Eq. (20), r_s is the radius of the orbit; μ is the Earth gravitational constant; M_s is the spacecraft mass; and $m_t = \rho_t A_t L_t$ and ρ_t are the mass and the density of the LWT, respectively. Following previous works on bare tethers [6,7], the average current intensity i_{av} will be presented as a function of the ratio L/L^*, where

$$L^* \equiv \left(\frac{2A_t}{p_t}\right)^{2/3}\left(\frac{9\pi^2 m_e \sigma_t^2 E_m}{128 e^3 N_0^2}\right)^{1/3} \tag{21}$$

is a characteristic dimension that gauges ohmic effects.

Figure 6 shows i_{av} versus L/L^* for the parameters discussed in Sec. II.B (cases 1–3). Similar to Fig. 4, solid lines correspond to i_{av} values computed with the j_{LWT}–φ_p curves obtained from the Vlasov–Poisson solver, and dashed lines correspond with the model of [12] extended with photoemission. For low emission (case 2), the differences are notable (above 20%). However, for high emission (case 3), the agreement is better than 2% (except in the limit $L/L^* \to 0$, which is not interesting for tether applications). Although the numerical and analytical j_{LWT}–φ_p curves exhibit greater differences for high emission because the SCL potential range is broader (see Fig. 4), the i_{av} curve shows the worst agreement for low emission. This result is explained by the fact that i_{av} is obtained after an integration along the tether. For high emission, the OML electron collection for $\varphi_p > 0$ and the RD emission at monotonic potential for $\varphi_p < 0$ contribute most to the i_{av} integral and, among such bias ranges, the agreement between both models is good. We also checked that ohmic effects can be safely ignored for cases 1 and 2. However, in case 3, such a simplification would overestimate the current up to 10% for the range of tether lengths considered in the analysis.

It is remarkable that the LWT efficiencies obtained from the numerical J_{LWT}–φ_p curves are above the one obtained with the analytical model of [12]. Therefore, such an analytical model is
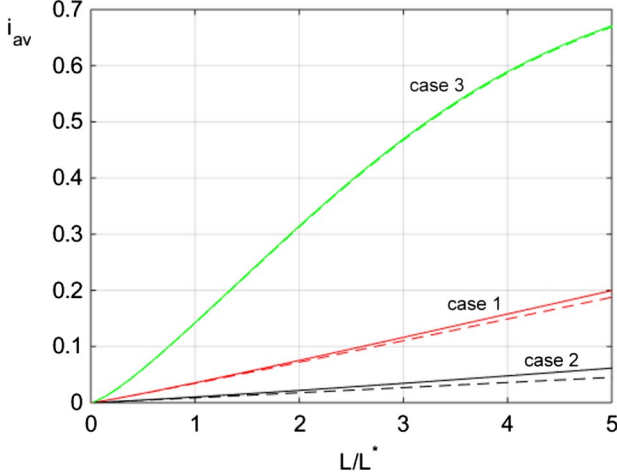
Fig. 6 i_{av} **versus** L/L^* **obtained from the numerical (solid) and analytical (dashed) models.**

appropriate to carry out a conservative analysis in preliminary studies. On the other hand, tether efficiency is enhanced by increasing the emission level (see Fig. 6). The normalized average current i_{av} increases with $\beta_{th} + \beta_{ph}$, and therefore with currents J_{th} and J_{ph} [see Eq. (15)]. LWTs should be manufactured with the lowest achievable work function coating and with a high photoelectric yield.

Tape tethers exhibit much better performance and are more robust against space debris impacts than round tethers [32]. They are more efficient because, for equal mass and length, tapes have larger perimeters and smaller L^* due to the factor $(A_t/p_t)^{2/3}$ in Eq. (21). However, in order to find more accurate results, the relation $J(\Phi_p)$ for tapes is needed. This can be done by adapting the two-dimensional stationary Vlasov–Poisson solver of [33] to include electron emission. An approximate alternative is to make the perimeter and cross-sectional-area replacements $2\pi R \rightarrow 2w_t$ and $\pi R^2 \rightarrow w_t h_t$, with w_t and h_t as the width and the thickness of the tape. Note that, in the OML regime, the collected current just depends on the perimeter [34], and the same approximation is accurate for tether cathodic points with monotonic potential. However, the limit of validity of the OML [20], the emitted current within the SCL regime, and the monotonic/nonmonotonic transition φ_p value must be determined anew for every cross section. As an example, we can make a first estimation of the deorbit performance of an aluminum tape with dimensions of $L_t = 2$ km, $w_t = 2$ cm and $h_t = 50$ μm, mass of $m_t = \rho_t L_t w_t h_t = 5.4$ kg, and a spacecraft with a mass of $M_s = 500$ kg and orbiting at 800 km of altitude. For the parameters of cases 1–3, one finds $L/L^* \approx 1, 4.8$, and 4.8; and Fig. 6 gives $i_{av} \approx 0.03, 0.06$, and 0.65. Equation (20) provides a decay rate of 2.3, 4.2, and 46 km/day.

Table 2   Candidates for LWT substrate

Material	ρ_t, kg/m³	σ_t, Ω^{-1} m^{-1}	T_m, K
Al (1100-H19)	2700	$3.54 \cdot 10^7$	920
BeCu (C17500)	8600	$2.61 \cdot 10^7$	1300

Table 3   Candidates for LWT coating

Material	W, eV
C12A7: e$^-$	0.6, 0.76, 2.1, 2.4
BaO-W	2.1
CeB$_6$	2.5
LaB$_6$	2.7

IV.   LWT Material Selection

The LWT model presented in Secs. II and III highlights the key design parameters that control the performance of LWTs. This information can be used to select the most promising materials for the tether substrate and its coating. In particular, according to Eqs. (6) and (8), the tether material should have a low work function to enhance the thermionic and the photoelectric emissions and should sustain high temperature without losing mechanical properties. Equation (20) shows that the substrate of the LWT should have a high value for the ratio σ_t/ρ_t. On the other hand, because the electron emission is greatly enhanced by the tether temperature (see Fig. 3), a high melting temperature T_m is also desirable. The properties of two possible materials, Al 1100-H19 and Beryllium-Copper (BeCu) C17500 alloys, are presented in Table 2. The decision between these two materials is linked to the properties of the thermionic coating. If the work function is low enough and good emission levels are possible at, say, $T \approx 500$ K, then Al is a better choice (due to the larger σ_t/ρ_t ratio). However, if the tether should operate at a higher temperature to stimulate the thermionic emission, then a BeCu tether is required due to its higher melting point.

The requirements for the coating are quite demanding because it involves the work function value, optical properties like absorptivity and emissivity, and its stability in a tough space environment. Table 3 shows the work function of some thermionic materials. The most promising is the C12A7: e$^-$ electride [35], which combines exceptional characteristics. Although comprising two insulating oxides, it exhibits high electronic conductivity at room temperature, is chemically inert, and its work function is extremely low. Two research groups working in electric propulsion measured extremely low-work-function values (0.76 eV [36] and 0.6 eV [37]), but the intrinsic work function should be higher (2.1 eV [38] and 2.4 eV [39]). Besides the work function, the final optical properties of the coated tether surface are also critical. In particular, as shown in Eq. (10), the ratio $\alpha_{abs}/\epsilon_{em}$ should be within a certain range to guarantee that the LWT operates at the required temperature.

Besides manufacturing issues, there are three testing activities that are required to improve the confidence in the model. First, the relationship $J(\Phi_p)$ could be determined experimentally by studying the collected and emitted currents of biased LWT samples in a plasma chamber. Second, the photoelectric yield $Y_{ph}(E)$ may be determined experimentally to predict the response of a LWT irradiated by sunlight. Third, testing of the optical properties α_{abs} and ϵ_{em} is also needed. These are the main elements that dictate whether the cathodic contact of the LWT with the plasma is efficient and if the concept is feasible.

V.   Conclusions

The analysis of this work shows that the photoelectric effect can be used by low-work-function electrodynamic tethers to achieve good cathodic contact, thus avoiding the use of active elements like hollow cathodes. If the tether is coated with a photosensitive compound, then the cathodic segment of the tether would work as a passive photocathode under the natural illumination of the Sun. Whether photoemission is dominant, negligible, or comparable to thermionic emission depends on tether temperature, work function, and photoelectric yield. As shown in Fig. 3, higher emission levels are reached in the parametric domain where the thermionic emission is dominant. However, such a scenario requires a tether temperature and a work function that are very demanding for the conductive substrates and coatings. The state of the art of low-work-function materials indicates that a low-W tether (LWT) with comparable thermionic and photoelectric emissions may be more feasible in the short term. The analysis showed that for typical conditions for low Earth orbit, tether temperature $T \approx 500$ K, and work function $W = 1.5$ eV, both emissive mechanisms are comparable and present an efficiency that is similar to the electron collection. In this case, the photoelectric and thermionic effects should be included in the model to accurately determine the Lorentz force.

Current and voltage profiles along LWTs have been computed with a model that incorporates orbital-motion theory along the full

tether. The calculations, which give a rigorous treatment of the current emission within the space-charge-limited segment, show that previous analytical models are slightly conservative. Therefore, their implementations are fully justified for preliminary mission design purposes. The model introduced in this work could be used by tether flight simulators, aimed at the performance determination of LWTs with thermionic and photoelectric effects. However, such application needs the development of a large dataset with the current/voltage characteristics obtained from the orbital-motion theory for a wide range of conditions, including tether geometry and environmental variables. Such a work would also have applications to emissive and Langmuir probes applied to plasma diagnostics.

Appendix: Orbital-Motion Theory Results

For a cylindrical probe immersed at rest in a stationary and collisionless plasma, the Vlasov equation conserves the angular momentum, the energy, and the particle distribution functions. These conservation laws are used to write the normalized particle densities, $n_{e,i}(\rho) \equiv N_{e,i}(r)/N_0$ and $n_{ph,th}(\rho) \equiv N_{ph,th}(r)/N_{0ph,th}$, as a function of the normalized radial distance $\rho = r/R$ and electrostatic potential $\varphi(\rho) = e\Phi(r)/kT_e$ (see details in [17]):

$$n_\alpha(\rho) = 2H_\alpha \int_{u_{\alpha\rho}^*}^\infty \frac{\exp(-\epsilon_\alpha)}{\pi} \arcsin\left(\frac{l_\alpha^*}{l_{\alpha\rho}}\right) d\epsilon_\alpha$$
$$- H_\alpha \int_{u_\alpha^*}^\infty \frac{\exp(-\epsilon_\alpha)}{\pi} \arcsin\left(\frac{l_\alpha^*}{l_{\alpha\rho}}\right) d\epsilon_\alpha \qquad (A1)$$

In Eq. (A1), the subscript α denotes $\alpha = e, i$, ph, and th, and we introduced the following functions: $H_{e,i} = 1$, $H_{ph,th} = 2$, $l_{\alpha\rho}^2(\rho, \epsilon_\alpha) = \rho^2[\epsilon_\alpha - u_{\alpha\rho}(\rho)]$, $u_{i\rho} = \varphi/\delta_i$, $u_{e\rho} = -\varphi$, $u_{ph\rho} = -(\varphi - \varphi_p)/\delta_{ph}$, and $u_{th\rho} = -(\varphi - \varphi_p)/\delta_{th}$, where

$$u_\alpha^* \equiv \max\{u_\alpha(\rho'): 1 \leq \rho' < \infty\} \qquad (A2)$$

$$l_\alpha^*(\epsilon_\alpha) \equiv \min\{l_{\alpha\rho}(\rho', \epsilon_\alpha): 1 \leq \rho' < \infty\} \qquad (A3)$$

and

$$u_{\alpha\rho}^*(\rho) \equiv \max\{u_\alpha(\rho')\} \qquad (A4)$$

$$l_{\alpha\rho}^*(\rho, \epsilon_\alpha) \equiv \min\{l_{\alpha\rho}(\rho', \epsilon_\alpha)\} \qquad (A5)$$

with $1 \leq \rho' \leq \rho$ for $\alpha = $ ph and th, and $\rho \leq \rho' < \infty$ for $\alpha = e$ and i. The substitution of Eq. (A1) in Poisson's equation

$$\frac{1}{\rho}\frac{d}{d\rho}\left(\rho\frac{d\varphi}{d\rho}\right) = -\rho_0^2(n_i - n_e - \beta_{ph}n_{ph} - \beta_{th}n_{th}) \qquad (A6)$$

yields an integrodifferential equation for $\varphi(\rho)$ that should be solved with the boundary conditions $\varphi(1) = \varphi_p$ and $\varphi \to 0$ as $\rho \to \infty$. Once solved (for instance, using a finite element method combined with a Newton algorithm [17]), the total current J in Eq. (1) is

$$\frac{J}{J_0} \equiv j_{LWT}(\varphi_p) = \sum_\alpha \frac{2G_\alpha}{\sqrt{\pi}} \int_{u_\alpha^*}^\infty l_\alpha^*(\epsilon_\alpha) \exp(-\epsilon_\alpha) d\epsilon_\alpha \qquad (A7)$$

with $J_0 \equiv eN_0\sqrt{k_BT_e/2\pi m_e}$ as the random electron thermal current. The sum should be extended to the four species ($\alpha = e, i$, ph, th), and we define the constants $G_i = -\sqrt{\delta_i/\mu_i}$, $G_e = 1$, $G_{th} = -2\beta_{th}\sqrt{\delta_{th}}$, $G_{ph} = -2\beta_{ph}\sqrt{\delta_{ph}}$, and $\mu_i = m_i/m_e$.

Acknowledgments

References

[1] Liou, J., and Johnson, N., "A Sensitivity Study of the Effectiveness of Active Debris Removal in LEO," *Acta Astronautica*, Vol. 64, Nos. 2–3, Jan. 2009, pp. 236–243.
doi:10.1016/j.actaastro.2008.07.009

[2] Liou, J. C., Rossi, A., Krag, H., Xavier James Raj, M., Anilkumar, K., Hanada, T., and Lewis, H., "Stability of the Future LEO Environment," Inter-Agency Space Debris Coordination Committee, Working Group 2, Action Item 27.1, Vol. 8, Rept. IADC-12-08, Rev. 1, Jan. 2013.

[3] Carroll, J. A., "Tether Applications in Space Transportation," *Acta Astronautica*, Vol. 13, No. 4, 1986, pp. 165–174.
doi:10.1016/0094-5765(86)90061-5

[4] Grossi, M. D., "Tether History and Historiography," *2nd International Conference on Tether in Space*, Consiglio Nazionale delle Ricerche, Venice, Italy, 1987, pp. 3–8.

[5] Cosmo, M., and Lorenzini, E. C., *Tethers in Space Handbook*, 3rd ed., NASA CR-97-206807, 1997.

[6] Sanmartin, J. R., Martinez-Sanchez, M., and Ahedo, E., "Bare Wire Anodes for Electrodynamic Tethers," *Journal of Propulsion Power*, Vol. 9, No. 3, 1993, pp. 353–360.
doi:10.2514/3.23629

[7] Ahedo, E., and Sanmartn, J. R., "Analysis of Bare-Tether Systems for Deorbiting Low-Earth-Orbit Satellites," *Journal of Spacecraft and Rockets*, Vol. 39, No. 2, March 2002, pp. 198–205.
doi:10.2514/2.3820

[8] Bombardelli, C., Zanutto, D., and Lorenzini, E. C., "Deorbiting Performance of Bare Electrodynamic Tethers in Inclined Orbits," *Journal of Guidance, Control, and Dynamics*, Vol. 36, No. 5, 2013, pp. 1550–1556.
doi:10.2514/1.58428

[9] Sanmartin, J. R., Sanchez-Torras, A., Khan, S. B., Sanchez-Arriaga, G., and Charro, M., "Optimum Sizing of Bare-Tape Tethers for De-Orbiting Satellites at End of Mission," *Advances in Space Research*, Vol. 56, No. 7, 2015, pp. 1485–1492.
doi:10.1016/j.asr.2015.06.030

[10] Williams, J. D., Sanmartín, J. R., and Rand, L. P., "Low Work-Function Coating for an Entirely Propellantless Bare Electrodynamic Tether," *IEEE Transactions on Plasma Science*, Vol. 40, No. 5, May 2012, pp. 1441–1445.
doi:10.1109/TPS.2012.2189589

[11] Sánchez-Arriaga, G., Chen, X., and Lorenzini, E., "Optimal Design and Deorbiting Performance of Thermionic Bare Tethers in Geostationary Transfer Orbits," *Journal of Propulsion and Power*, Vol. 33, No. 2, 2017, pp. 425–432.
doi:10.2514/1.B36202

[12] Chen, X., and Sanmartn, J. R., "Bare-Tether Cathodic Contact Through Thermionic Emission by Low-Work-Function Materials," *Physics of Plasmas*, Vol. 19, No. 7, July 2012, Paper 073508.
doi:10.1063/1.4736987

[13] Sanmartín, J. R., Chen, X., and Sanchez-Arriaga, G., "Analysis of Thermionic Bare Tether Operation Regimes in Passive Mode," *Physics of Plasmas*, Vol. 24, No. 1, 2017, Paper 013515.
doi:10.1063/1.4974764

[14] Chen, X., "Low-Work-Function Thermionic Emission and Orbital-Motion-Limited Ion Collection at Bare-Tether Cathodic Contact," Ph.D. Thesis, Univ. Politécnica de Madrid, Madrid, 2015.

[15] Chen, X., and Sanmartín, J. R., "Low Work-Function Thermionic Emission and Orbital-Motion-Limited Ion Collection at Bare-Tether Cathodic Contact," *Physics of Plasmas*, Vol. 22, No. 5, 2015, Paper 053504.
doi:10.1063/1.4919945

[16] Drell, S. D., Foley, H. M., and Ruderman, M. A., "Drag and Propulsion of Large Satellites in the Ionosphere: An Alfvén Propulsion Engine in Space," *Physical Review Letters*, Vol. 14, No. 6, 1965, pp. 171–175.
doi:10.1103/PhysRevLett.14.171

[17] Chen, X. C., and Sanchez-Arriaga, G., "Orbital Motion Theory and Operational Regimes for Cylindrical Emissive Probes," *Physics of Plasmas*, Vol. 24, No. 2, 2017, Paper 023504.
doi:10.1063/1.4975088

[18] Laframboise, J. G., "Theory of Spherical and Cylindrical Langmuir Probes in a Collisionless, Maxwellian Plasma at Rest," Ph.D. Thesis, Univ. of Toronto, Toronto, 1966.

[19] Sánchez-Arriaga, G., and Sanmartn, J. R., "Relativistic Current Collection by a Cylindrical Langmuir Probe," *Physics of Plasmas*, Vol. 19, No. 6, June 2012, Paper 063506.
doi:10.1063/1.4729662

[20] Sanmartín, J. R., and Estes, R. D., "The Orbital-Motion-Limited Regime of Cylindrical Langmuir Probes," *Physics of Plasmas*, Vol. 6, No. 1, Jan. 1999, pp. 395–405.
doi:10.1063/1.873293

[21] Sanmartin, J. R., Charro, M., Pelaez, J., Tinao, I., Elaskar, S., Hilgers, A., and Martinez-Sanchez, M., "Floating Bare Tether as Upper Atmosphere Probe," *Journal of Geophysical Research: Space Physics*, Vol. 111, No. A11, Nov. 2006, Paper A11310.
doi:10.1029/2006JA011624

[22] Jensen, K. L., Feldman, D. W., Moody, N. A., and O'Shea, P. G., "A Photoemission Model for Low Work Function Coated Metal Surfaces and its Experimental Validation," *Journal of Applied Physics*, Vol. 99, No. 12, June 2006, Paper 124905.
doi:10.1063/1.2203720

[23] ASTM E490-00a, "Standard Solar Constant and Zero Air Mass Solar Spectral Irradiance Tables," ASTM International, West Conshohocken, PA, 2014, www.astm.org.

[24] Hinteregger, H. E., Hall, L. A., and Schmidtke, G., "Solar XUV Radiation and Neutral Particle Distribution in July 1963 Thermosphere," *Space Research*, Vol. 5, 1965, p. 1175.

[25] Fowler, R. H., "The Analysis of Photoelectric Sensitivity Curves for Clean Metals at Various Temperatures," *Physical Review*, Vol. 38, No. 1, July 1931, pp. 45–56.
doi:10.1103/PhysRev.38.45

[26] Dubridge, L. A., *New Theories of the Photoelectric Effect*, Hermann and Cie, Paris, 1935.

[27] Berglund, C. N., and Spicer, W. E., "Photoemission Studies of Copper and Silver: Experiment," *Physical Review*, Vol. 136, No. 4A, Nov. 1964, pp. A1044–A1064.
doi:10.1103/PhysRev.136.A1044

[28] Grard, R. J. L., "Properties of the Satellite Photoelectron Sheath Derived from Photoemission Laboratory Measurements," *Journal of Geophysical Research*, Vol. 78, No. 16, June 1973, pp. 2885–2906.
doi:10.1029/JA078i016p02885

[29] Choiniere, E., "Theory and Experimental Evaluation of a Consistent Steady-State Kinetic Model for Two-Dimensional Conductive Structures in Ionospheric Plasmas with Application to Bare Electrodynamic Tethers in Space," Ph.D. Thesis, Univ. of Michigan, Ann Arbor, MI, 2004.

[30] Sánchez-Arriaga, G., "A Direct Vlasov Code to Study the Non-Stationary Current Collection by a Cylindrical Langmuir Probe," *Physics of Plasmas*, Vol. 20, No. 1, Jan. 2013, Paper 013504.
doi:10.1063/1.4774398

[31] Sánchez-Arriaga, G., and Pastor-Moreno, D., "Direct Vlasov Simulations of Electron-Attracting Cylindrical Langmuir Probes in Flowing Plasmas," *Physics of Plasmas*, Vol. 21, No. 7, July 2014, Paper 073504.
doi:10.1063/1.4889732

[32] Khan, S. B., and Sanmartin, J. R., "Survival Probability of Round and Tape Tethers Against Debris Impact," *Journal of Spacecraft and Rockets*, Vol. 50, No. 3, May 2013, pp. 603–608.
doi:10.2514/1.A32383

[33] Choiniere, R., and Gilchrist, B. E., "Self-Consistent 2-D Kinetic Simulations of High-Voltage Plasma Sheaths Surrounding Ion-Attracting Conductive Cylinders in Flowing Plasmas," *IEEE Transactions on Plasma Science*, Vol. 35, No. 1, Feb. 2007, pp. 7–22.
doi:10.1109/TPS.2006.889300

[34] Laframboise, J. G., and Parker, L. W., "Probe Design for Orbit-Limited Current Collection," *Physics of Fluids*, Vol. 16, No. 5, 1973, pp. 629–636.
doi:10.1063/1.1694398

[35] Toda, Y., Matsuishi, S., Hayashi, K., Ueda, K., Kamiya, T., Hirano, M., and Hosono, H., "Field Emission of Electron Anions Clathrated in Subnanometer-Sized Cages in $[Ca24Al28O64]^{4+}(4e^-)$," *Advanced Materials*, Vol. 16, No. 8, 2004, pp. 685–689.
doi:10.1002/(ISSN)1521-4095

[36] Rand, L. P., "A Calcium Aluminate Electride Hollow Cathode," Ph.D. Thesis, Colorado State Univ., Fort Collins, CO, 2014.

[37] Bock, D., Drobny, C., Laufer, P., Kössling, M., and Tajmar, M., "Development and Testing of Electric Propulsion Systems at TU Dresden," *52nd AIAA/SAE/ASEE Joint Propulsion Conference*, AIAA Paper 2016-4848, July 2016.
doi:10.2514/6.2016-4848

[38] Toda, Y., Kim, S. W., Hayashi, K., Hirano, M., Kamiya, T., Hosono, H., Haraguchi, T., and Yasuda, H., "Intense Thermal Field Electron Emission from Room-Temperature Stable Electride," *Applied Physics Letters*, Vol. 87, No. 25, Dec. 2005, Paper 254103.
doi:10.1063/1.2149989

[39] Toda, Y., Yanagi, H., Ikenaga, E., Kim, J. J., Kobata, M., Ueda, S., Kamiya, T., Hirano, M., Kobayashi, K., and Hosono, H., "Work Function of a Room-Temperature, Stable Electride [Ca24Al28O64]4+(e Ű)4," *Advanced Materials*, Vol. 19, No. 21, 2007, pp. 3564–3569.
doi:10.1002/(ISSN)1521-4095

G. G. Spanjers
Associate Editor